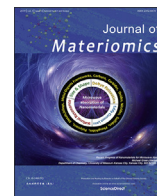




Contents lists available at ScienceDirect

Journal of Materiomics

journal homepage: www.journals.elsevier.com/journal-of-materiomics/

Microstructure and composition engineering Yb single-filled CoSb₃ for high thermoelectric and mechanical performances

HPSTAR
872-2019



Zhenxing Zhou^{a,1}, Matthias T. Agne^{b,1}, Qihao Zhang^{c,***}, Shun Wan^d, Qingfeng Song^{c,e}, Qing Xu^{c,e}, Xiaofang Lu^a, Shijia Gu^a, Yuchi Fan^f, Wan Jiang^{a,g}, Gerald Jeffrey Snyder^{b,**}, Lianjun Wang^{a,*}

^a State Key Laboratory for Modification of Chemical Fibers and Polymer Materials, College of Materials Science and Engineering, Donghua University, Shanghai, 201620, China

^b Department of Materials Science and Engineering, Northwestern University, Evanston, IL, 60208, USA

^c State Key Laboratory of High Performance Ceramics and Superfine Microstructure, Shanghai Institute of Ceramics, Chinese Academy of Sciences, Shanghai, 200050, China

^d Center for High Pressure Science and Technology Advanced Research (HPSTAR), Shanghai, 201203, China

^e University of Chinese Academy of Sciences, 19 Yuquan Road, Beijing, 100049, China

^f Institute of Functional Materials, Donghua University, Shanghai, 201620, China

^g School of Material Science and Engineering, Jingdezhen Ceramic Institute, Jingdezhen, 333000, China

ARTICLE INFO

Article history:

Received 2 March 2019

Received in revised form

18 April 2019

Accepted 23 April 2019

Available online 27 April 2019

Keywords:

Skutterudites

Thermoelectric material

Compositional complexity

Microstructure engineering

Cryogenic grinding

ABSTRACT

A broad tunability of the thermoelectric and mechanical properties of CoSb₃ has been demonstrated by adjusting the composition with the addition of an increasing number of elements. However, such a strategy may negatively impact processing repeatability and composition control. In this work, single-element-filled skutterudite is engineered to have high thermoelectric and mechanical performances. Increased Yb filling fraction is found to increase phonon scattering, whereas cryogenic grinding contributes additional microstructural scattering. A peak zT of 1.55 and an average zT of about 1.09, which is comparable to the reported results of multiple-filled SKDs, are realized by the combination of simple composition and microstructure engineering. Furthermore, the mechanical properties of Yb single-filled CoSb₃ skutterudite are improved by manipulation of the microstructure through cryogenic grinding. These findings highlight the realistic prospect of producing high-performance thermoelectric materials with reduced compositional complexity.

© 2019 The Chinese Ceramic Society. Production and hosting by Elsevier B.V. This is an open access article under the CC BY-NC-ND license (<http://creativecommons.org/licenses/by-nc-nd/4.0/>).

1. Introduction

The increase in world energy demand as well as environmental concerns have attracted attention from the government, academia, and industry all over the world. Thermoelectric (TE) materials, capable of converting heat into electricity directly, have potential to contribute to alternative-energy production through waste heat recovery [1,2]. The conversion efficiency of TE materials is related to

the dimensionless figure of merit zT , which is defined as $zT = \alpha^2 \sigma T / \kappa_{\text{tot}}$. α , σ , T and κ_{tot} are the Seebeck coefficient, electrical conductivity, absolute temperature, and the total thermal conductivity, respectively. Generally, $\kappa_{\text{tot}} = \kappa_{\text{ele}} + \kappa_{\text{lat}}$ consists of the electronic thermal conductivity, κ_{ele} and the lattice thermal conductivity, κ_{lat} . Higher zT corresponds to a higher conversion efficiency. Therefore, the challenge to developing efficient TE materials with high zT is to achieve simultaneous enhancement in the electrical properties (power factor ($\alpha^2 \sigma$)) and reduction in the thermal conductivity.

CoSb₃-based skutterudites (SKDs) are promising candidates for TE power generation applications in the intermediate temperature region (550–900 K), thanks to a reasonably large band gap, high carrier mobility, inexpensive and environmentally friendly constituent elements, and good mechanical properties [3]. They have cage-like voids in their crystal structure, which can be filled with loosely bound foreign atoms that both act to improve electronic

* Corresponding author.

** Corresponding author.

*** Corresponding author.

E-mail addresses: zhangqh@mail.sic.ac.cn (Q. Zhang), jeff.snyder@northwestern.edu (G.J. Snyder), wanglj@dhu.edu.cn (L. Wang).

Peer review under responsibility of The Chinese Ceramic Society.

¹ These authors contributed equally to this work.

transport properties and strongly scatter phonons to suppress the κ_{lat} . Previous studies have shown that the voids in the CoSb₃-based skutterudite alloys can be filled with different kinds of guest atoms, such as the rare-earth [4–7], alkaline-earth [8], and alkaline-metal [9]. Besides single-element filling, it is found that an even greater reduction in κ_{lat} and increase in zT can be achieved by filling multiple chemically distinct atoms into the voids of the skutterudite. In this case, each filler atom represents a phonon resonance scattering center with a particular frequency, scattering phonon modes that have frequencies close to the local resonant frequency [10]. As a result, the maximum zT was improved to 1.3–1.4 in double-element-filled SKDs [10–12] and over 1.5 in three-element-filled SKDs [13,14]. However, the multiple-element-filled high-performance SKDs have not been used for TE devices and practical application, mainly due to trouble with repeatability in large-scale production and difficulty in precise composition control, since small changes in the filling atom fraction can influence the power factor and the thermal conductivity [15]. Alternatively, TE performance may be improved by engineering the microstructure of a system that is not compositionally complex. This approach is more conducive for the long-term sustainability of high-performing materials and device applications.

To improve thermoelectric performance there is a concerted effort to reduce κ_{lat} towards the amorphous limit [16–18]. In addition to phonon scattering, it is desirable to have low phonon group velocity (speed of sound). Recent studies have shown that speed of sound can be controlled by composition and microstructure [19,20]. Thus, combining the effects of phonon scattering processes and reducing phonon group velocity is an effective strategy for reducing κ_{lat} . At the same time, electronic transport is relatively unaffected by microstructure because the carrier mean free path is smaller than the scales of typical microstructural features, leading to the possibility of high zT [18].

Fewer constituent elements and more repeatable performance make the single-element-filled SKDs the optimal choice for the preparation of TE devices [15,21,22]. Among all the filling elements, Yb is one of the most effective to lower κ_{lat} due to its heavy atomic mass and small ionic radius, which results in a low rattling frequency of $\sim 42 \text{ cm}^{-1}$ in CoSb₃ [6]. Nolas et al. first reported zT of 1.0 at 600 K for Yb filled n-type Yb_{0.19}Co₄Sb₁₂ compound in the year 2000 [4]. In the following years, the maximum zT for Yb filled n-type CoSb₃ has stagnated around 1.2 despite various authors have reported substantially different transport properties for a wide range of Yb filling fractions [6,23–26]. However, engineering of its microstructure is not fully studied.

In this work, we use cryogenic grinding (CG) and spark plasma sintering (SPS) in the fabrication of n-type Yb-filled CoSb₃ to achieve high thermoelectric and mechanical performance. Optimization of the filling fraction leads to high power factors over a broad temperature range and a suppression of lattice thermal conductivity. Consequently, a peak zT of 1.55 at 825 K and an average zT of around 1.09 from 300 to 875 K are realized, comparable to the reported results of multiple-filled SKDs. Simultaneously, Vickers hardness, fracture toughness, and three-point flexural strength are all increased, thus granting benefits for material processing and device integration.

2. Experimental

2.1. Material synthesis

Polycrystalline n-type Yb_xCo₄Sb₁₂ ingots were synthesized by the melting and annealing method. Co shot (99.8%, Alfa Aesar), Sb shot (99.999%, Chengdu Chemphys Chemical Industry, China) and Yb shot (99.9%, Alfa Aesar) were stoichiometrically weighed and

put into a graphite crucible, and then sealed within a quartz tube under vacuum. The sealed quartz tube was put into a vertical tube furnace and heated to 1080 °C for 24 h and then quenched in a supersaturated salt water solution. Then, the quenched quartz tube was annealed at 700 °C for 168 h to form the stable crystallographic phase. The obtained ingots were then cleaned, crushed into coarse particles and milled by hand into powders in an agate mortar. The hand-milled powders were used as the starting material.

A cryogenic grinding (CG) machine (SPEX Sample Prep 6770 Freezer/Mill, TECH-Knowledge International Co., California, USA) was subsequently used to further process the hand-milled powders. After putting the coarse powders and the magnetic impactor into a microvial, the closed grinding vial was immersed in liquid nitrogen and milled at a speed of 7–10 cycles per second for different time (0 min, 15 min, 30 min, 60 min and 120 min, indicated as CG-0, CG-15, CG-30, CG-60 and CG-120, respectively). To prevent the oxidation, the microvial was sealed inside the glove box. After CG, the powders were then loaded into a cylindrical graphite die with a 10-mm inner diameter and sintered by spark plasma sintering (SPS, Dr. Sinter 725, Japan). The sintering temperature and dwell time are 923 K and 5 min, respectively. The consolidated samples were further annealed at 1023 K for 2 days.

2.2. Characterization

The phase identification and purity of all samples were investigated by X-ray diffraction (XRD, Rigaku D/Max-2550 PC, Japan) with Cu K α radiation at 40 kV and 200 mA. A field emission scanning electron microscopy (SEM, Hitachi S-4800, Japan) was utilized to characterize the morphology of the powders and the freshly-fractured surfaces of the bulk samples. The lineal intercept method was used to characterize the average grain size. The error in the average grain size estimation is about 20% of the mean. Transmission electron microscopy (TEM, JEOL 2100F, Japan) with selected area electron diffraction was used to study the microstructure of the bulk samples. The thermoelectric properties of all bulk samples were measured from 300 K to 873 K. The electrical resistivity and Seebeck coefficient were simultaneously measured using a ZEM-3 equipment (ULVAC-RIKO, Japan) under a helium atmosphere after samples were cut into rectangles of approximately $3 \times 3 \times 8 \text{ mm}^3$. The uncertainty of the electrical resistivity and Seebeck coefficient measurements is around 5%. The thermal conductivity (κ) was calculated by $\kappa = D \times C_p \times \rho_d$, where D is the thermal diffusivity measured by a laser flash apparatus (LFA 457, Netzsch, Germany), C_p is the specific heat measured on a differential scanning calorimeter (DSC, 204F1, Netzsch, Germany), and ρ_d is the density measured by the Archimedes method. The uncertainty of κ is estimated to be within 5%, considering the uncertainties for D , C_p and ρ_d . The combined uncertainties enable an uncertainty of less than 12% for zT . The Hall coefficient (R_H) was measured on a Hall effect test system Lakeshore 8404 (Lake Shore Cryotronics Inc, USA) with a magnetic field of 1.5 T and an electrical current of 100 mA.

The fracture toughness K_{IC} of the bulk samples was determined using a Vickers indentation fracture test apparatus. The K_{IC} was calculated by $K_{\text{IC}} = 0.016 \left(\frac{E}{HV} \right) \left(\frac{P}{c^{1.5}} \right)$ according to the half-penny-shaped crack model, where E is the Young's modulus, HV is the Vickers hardness, P is the applied indentation load, and c is the average half length of the crack. HV was obtained with a microhardness tester (HV-1000, Lunjie, China) under a test load of 1.96 N for 10 s. Twenty indentations were made at different locations on each polished sample to obtain an average HV value. The E was measured by a nanoindenter (XP, MTS, USA) with a depth of 300 nm. Twenty locations on each polished sample were tested to obtain an average E value. The c was measured under an optical

microscope. Three-point flexural tests were conducted using a desktop multi-functional material performance testing machine (DSII) at room temperature, with a span of 12–25 mm and a crosshead speed of 0.5 mm/min. The test bars used to determine the flexural strength had the dimension of 2 mm × 3 mm × 18 mm. The three-point flexural strength (σ_b) was calculated by $\sigma_b = 3PL / (2bh^2)$, where P is the maximum load before fracture, L is the actual span, b and h are the width and thickness of the sample. Each test was conducted on at least five samples and the results were averaged. Low temperature heat capacity measurements were done on a physical properties measurement system (PPMS-9, Quantum Design, USA) at temperatures between 3.3 K and 25 K (Table S1). The data was obtained using the relaxation method and collected during heating.

3. Results and discussion

3.1. Phase composition

XRD patterns for all bulk $\text{Yb}_{0.35}\text{Co}_4\text{Sb}_{12}$ samples with different CG time are shown in Fig. 1a. The main diffraction peaks for all samples correspond well to the JCPDS data card no. 65–3144 for cubic skutterudite (space group $Im\bar{3}$), which means that cryogenic grinding did not destroy the structure of the Yb-filled CoSb_3 matrix. However, all bulk samples show a trace amount of Yb_2O_3 . As seen from the inset of Fig. 1a, the main diffraction peak of (013) shifts to higher angles for the CG-60 and CG-120 samples, indicating a smaller lattice parameter. Increased filling fraction of Yb in skutterudite can expand the crystal lattice and lead to an increase in lattice parameter a . Tang et al. found that the lattice parameter for $\text{Yb}_x\text{Co}_4\text{Sb}_{12}$ can vary from $a = 9.03 \text{ \AA}$ to 9.07 \AA when the Yb filling fraction is increased from 0 to 0.5 [28]. As is shown in Fig. 1b, the a values correspond to the Yb filling fraction measured via EDS, in agreement with the general trend. The XRD results also suggest that the filling fraction is decreased for CG time longer than 30 min.

3.2. Microstructure

The SEM images of the nominal $\text{Yb}_{0.35}\text{Co}_4\text{Sb}_{12}$ powders after undergoing different cryogenic grinding times and the corresponding particle size distributions are shown in Fig. S1. It can be seen that the initial powders milled merely by hand mainly consists of micron-sized particles and the average particle size is about 2 μm . After cryogenic grinding, the particle size significantly decreases. For example, the particle size distribution becomes much narrower with an average size of approximately 50 nm (Fig. S1f)

after being ground for 120 min. Consequently, it is not surprising that the grain size of the consolidated bulk material is successively lower for longer cryogenic grinding times. From SEM images (Fig. 2a–e and S2) of the fractured surface of the sintered samples, it is possible to estimate the average grain size, \bar{d} , from the lineal intercept method [29]. The estimates of \bar{d} are summarized in Fig. 2f. Comparing the CG-0 sample ($\bar{d} = 12.6 \mu\text{m}$, Fig. 2a) to the CG-30 sample ($\bar{d} = 1.3 \mu\text{m}$, Fig. 2c), the average grain size is 10 times smaller in the latter. Importantly, these samples both have the same Yb filling fraction. Although the grain size is further decreased in the CG-60 ($\bar{d} = 0.8 \mu\text{m}$, Fig. 2d) and CG-120 ($\bar{d} = 0.3 \mu\text{m}$, Fig. 2e) samples, there is measurably less Yb in these materials (Fig. 1b).

As is known, SPS is a rapid and low-temperature sintering process, which can effectively suppress grain growth. Therefore, the CG/SPS method is well suited for engineering micro/nano-scaled microstructures (Fig. S2). Moreover, the volume ratio of pores decreases with increasing grinding time and the crystallized grains are closely packed, suggesting that the nano-scaled grains might be filled into the space between the micro-scaled grains (demonstrated in Figs. S2 and 2g), resulting in the higher density (7.41, 7.45, 7.54, 7.55 and 7.58 g/cm^3 , respectively). Fig. 2g is a TEM image of the CG-30 sample which shows the grain size, crystallinity and clean grain boundaries. From Fig. 2c, g, and i, it can be seen that the grain size is widely distributed, ranging from several nanometers to micrometers. The substantially coherent interfaces are beneficial for electron transport [30]. Moreover, the TEM mapping (Fig. 2h) combined with the high-resolution TEM analysis (Fig. 2i) also confirms the existence of Yb_2O_3 nanoparticles. The interplanar spacing of 4.26 \AA and 2.86 \AA corresponds to the (211) plane of Yb_2O_3 phase and (013) plane of CoSb_3 phase, respectively. The Yb_2O_3 nanoparticles may pin grain boundaries and help to prevent grain growth during densification, in addition to their proposed benefit in reducing thermal conductivity [31].

3.3. Thermoelectric properties

The electrical conductivities plotted as a function of the temperature for all bulk $\text{Yb}_{0.35}\text{Co}_4\text{Sb}_{12}$ samples with different CG time are shown in Fig. 3a. It is clear that the electrical conductivity (σ) decreases with temperature over the whole measured temperature range, showing degenerate conductive behavior. The σ of the CG-SPS is relatively unchanged up to 30 min CG time, and then decreases with increasing CG time. In order to elucidate the behavior, we measured Hall coefficient (R_H) at room temperature and plotted the hall mobility ($\mu_H = \sigma R_H$) as a function of carrier concentration ($n_H = -1/eR_H$, e is the free electron charge) in Fig. 3b. The μ_H - n_H

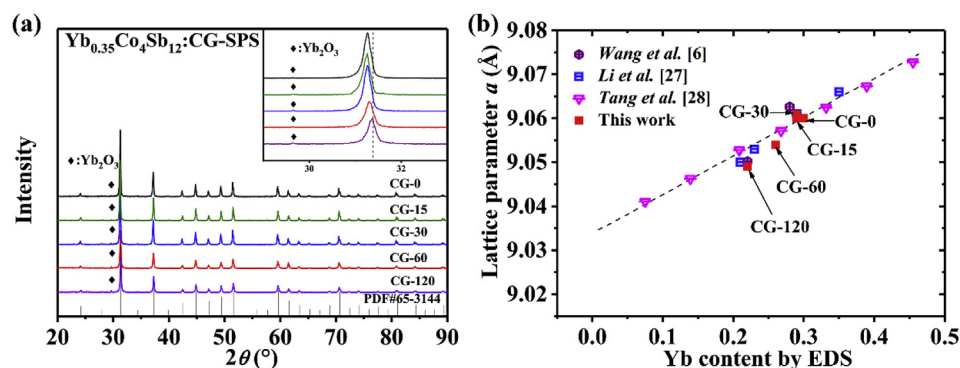


Fig. 1. Bulk nominal $\text{Yb}_{0.35}\text{Co}_4\text{Sb}_{12}$ samples with different CG time (a) XRD patterns and inset is the enlarged XRD patterns for (013) peak, (b) lattice parameter a as a function of Yb content determined by EDS in this work and several typical data from the Refs. [6,27,28]. The dashed line is a guide for the eyes.

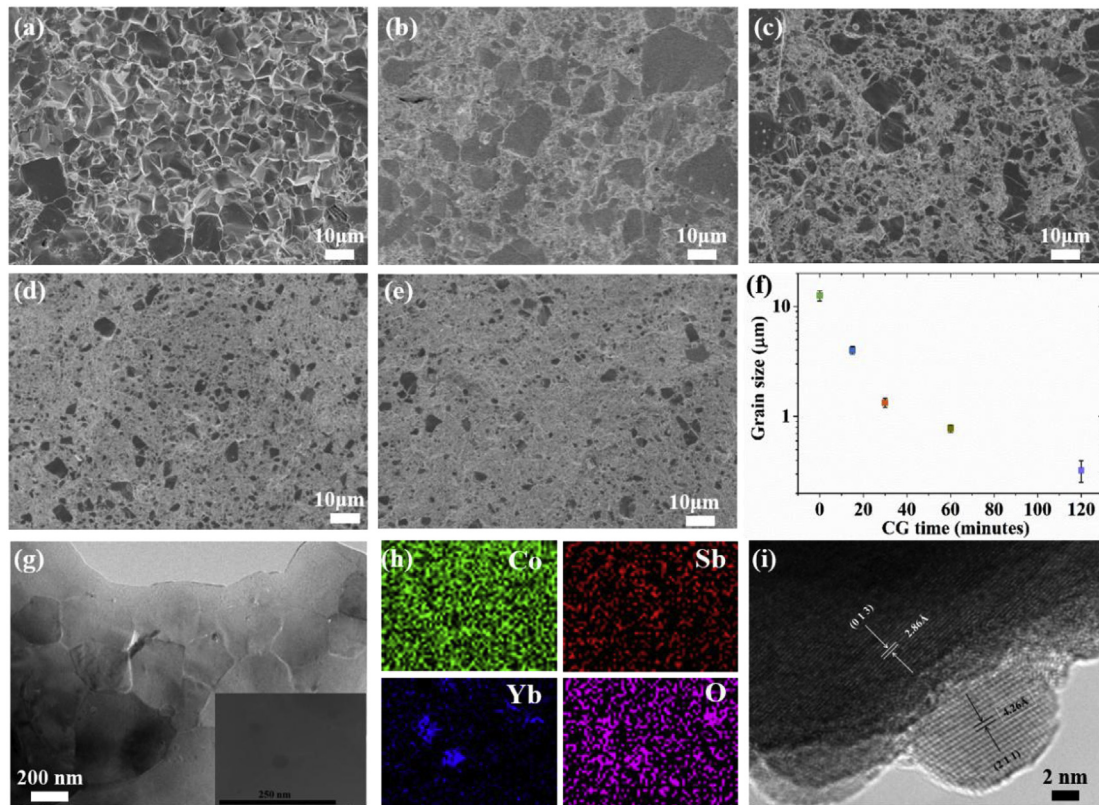


Fig. 2. SEM images of fractured surface of the sintered $\text{Yb}_{0.35}\text{Co}_4\text{Sb}_{12}$ samples obtained from cryogenic-ground powders for (a) 0 min, (b) 15 min, (c) 30 min, (d) 60 min and (e) 120 min. (f) The average grain size as function of CG time. (g) Typical TEM image of the CG-30 sample with the inset of a high-resolution TEM image. (h) The EDX mapping of the inset of (g). (i) High-resolution TEM analysis confirming the existence of Yb_2O_3 nanoprecipitates.

data for the CG-0, CG-15 and CG-30 samples agree with the trendline. However, the CG-60 and CG-120 samples have a lower μ_{H} than what is expected for their n_{H} . This indicates that short-time CG processing has a negligible influence on the carrier concentration (i.e., Yb composition) and carrier scattering. Longer CG times, however, result in a reduction in carrier concentration that is in agreement with the observed change in Yb composition (Fig. 1b), as well as an increase in carrier scattering from microstructural defects. Fig. 3c shows the temperature dependence of the Seebeck coefficient (α). The negative α demonstrates that electrons are the major carriers. It is notable that the absolute value of Seebeck coefficient increases with increasing temperature, typical of heavily doped semiconductors. As the CG time increases, the absolute Seebeck coefficient increases in accordance with the change in n_{H} due to Yb content (Fig. 1b).

As demonstrated previously [5], a three-band effective mass model can be used for electrical transport data analysis in CoSb_3 materials, providing valuable information for exploring mechanisms and optimizing TE performance. Based on the assumption of a single parabolic band and acoustic phonon scattering, the effective mass m^* was estimated using the measured n_{H} and Seebeck coefficient α . As shown in Fig. 3d, m^* increases gradually with increasing n_{H} , consistent with the three-band model which can be described empirically by the polynomial $\frac{m^*}{m_0} = -0.28x^4 + 1.8x^3 - 3.57x^2 + 3.2x + 0.24$, where $x = \log\left(\frac{n_{\text{H}}}{10^{18}}\right)$ and the polynomial is valid over the range $3 \times 10^{18} \text{ cm}^{-3} \leq n_{\text{H}} \leq 10^{21} \text{ cm}^{-3}$. The m^* - n_{H} data for all samples presented in this study agree with previous studies of filled CoSb_3 , within measurement error, indicating that the CG-SPS process has negligible influence on the electronic band

structure. The same model for m^* can be represented in the Pisarenko plot of Seebeck coefficient (α) vs. charge carrier concentration (n_{H} , measured by Hall effect). The decrease in Seebeck with carrier concentration (Fig. 3e) found here is consistent with prior results [6,8,9]. The Pisarenko curve obtained from the three-band model is empirically described by the polynomial $\alpha [\mu\text{V/K}] = -5.1x^3 + 45.7x^2 - 219x + 461$ and x has the same range and definition as before [5].

The power factors ($\alpha^2\sigma$) of all samples calculated from the Seebeck coefficients and electrical conductivities are shown in Fig. 3f. The CG-30 sample exhibits the highest power factor and achieves the high $\alpha^2\sigma$ of $>45 \mu\text{Wcm}^{-1}\text{K}^{-2}$ over a wide temperature range (450–850 K). The power factors of the CG-0 and CG-15 materials are somewhat lower, but are comparable considering measurement errors of ~ 5 – 10% . When extending the CG process time, Seebeck coefficients for the CG-60 and CG-120 samples increase because they have lower carrier concentrations, i.e. less Yb. However, the electrical conductivities are seriously-deteriorated because the mobility is substantially impacted at longer CG processing times. To verify the repeatability of the CG process, three separate CG-30 samples were prepared. Their electronic properties were measured to be within 6% of each other (see Fig. S3, Supporting Information).

The most dramatic influence of the CG processing on the transport properties is expected to be on the thermal conductivity. In Fig. 4a we plotted the temperature-dependent total thermal conductivity (κ_{tot}) of all bulk nominal $\text{Yb}_{0.35}\text{Co}_4\text{Sb}_{12}$ samples with different CG time. The lattice thermal conductivity (κ_{lat}) was calculated by subtracting the electronic thermal conductivity (κ_{ele})

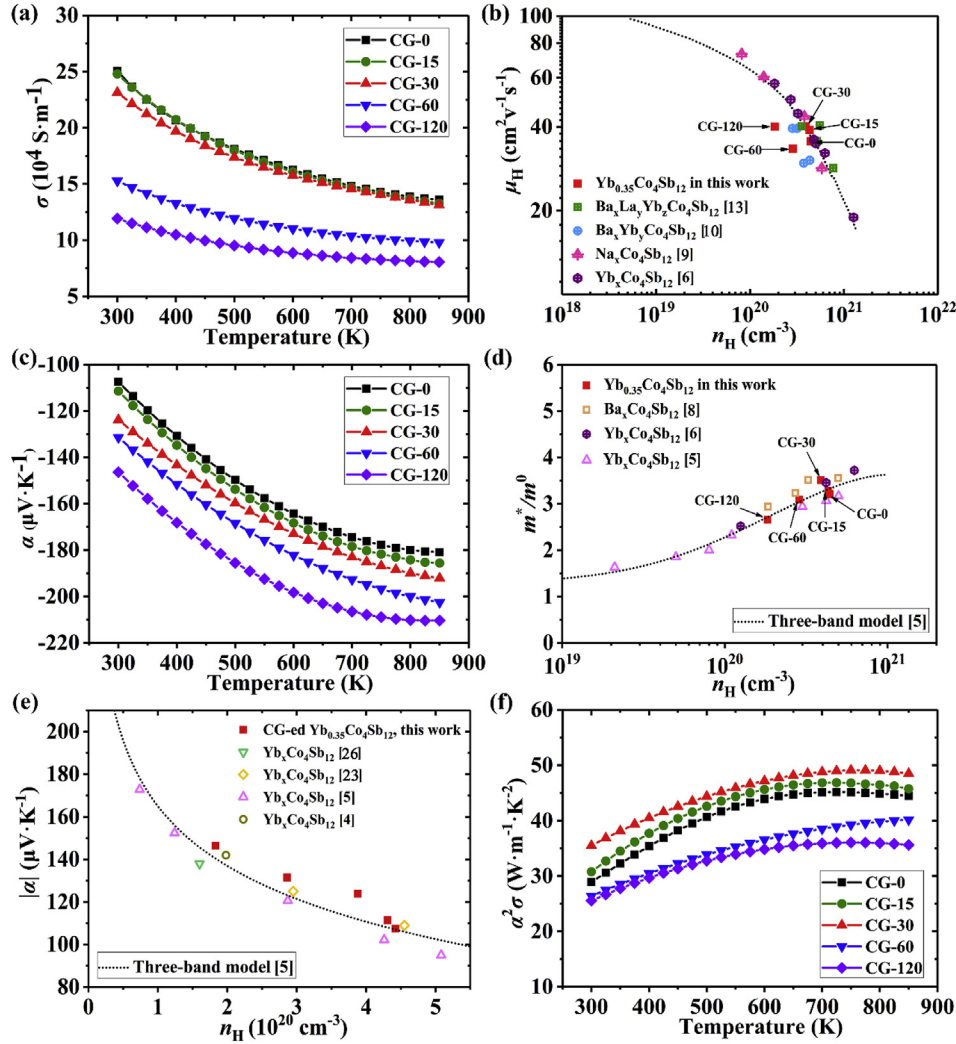


Fig. 3. Electrical transport properties of the bulk $\text{Yb}_{0.35}\text{Co}_4\text{Sb}_{12}$ samples with different CG time. (a) Temperature dependence of electrical conductivity (σ). (b) Hall mobility (μ_H) as a function of carrier concentration (n_H), and the dashed line shows the general trend. The CG-60 and CG-120 samples have lower mobility than what is expected for their carrier concentration. (c) Electron effective masses as a function of carrier concentration for CGed- $\text{Yb}_{0.35}\text{Co}_4\text{Sb}_{12}$ samples in this study and several typical data from the Refs. [5,6,8]. The dashed line represents the three-band model described in Ref. [5]. (d) Temperature dependence of Seebeck coefficient (α). (e) Absolute Seebeck coefficient as a function of hall carrier concentration for CGed- $\text{Yb}_{0.35}\text{Co}_4\text{Sb}_{12}$ samples in this study and several typical data from the Refs. [4,5,23,26]. Again, the dashed line represents the three-band model described in Ref. [5]. (f) Temperature dependence of power factor.

from the total thermal conductivity. κ_{ele} is estimated from the Wiedemann-Franz law ($\kappa_{\text{ele}} = L_0 \sigma T$), where L_0 is the Lorentz number, calculated here by employing a single parabolic band mode with the assumption of acoustic phonon scattering [15,24]. The temperature-dependent κ_{lat} is shown in Fig. 4b. We note that the κ_{lat} of the CG-0 sample is comparable to the result of Wang et al. [6] for nominally the same composition and having a comparable grain size. Although κ_{tot} continues to decrease with increasing CG processing time, κ_{lat} first decreases, reaching the minimum value of $\sim 1.3 \text{ W m}^{-1} \text{ K}^{-1}$ at 300 K after CG for 30 min, and then apparently increases with increasing CG time. However, the estimated κ_{lat} of the CG-60 and CG-120 materials is likely overestimated due to the strong influence of the grain boundaries on electrical conductivity.

The continued reduction in κ_{lat} between CG-0 and CG-30 samples can be ascribed to the change in microstructure (compare Fig. 2a and c), particularly the reduction in grain size. Previous work by Zong and Hanus et al. characterized the effective grain boundary resistance, R_K , of both n- and p-type CoSb_3 materials [21]. In this model, a polycrystalline material having average grain size \bar{d} has a

thermal conductivity lower than the bulk value κ_{bulk} (i.e. the intrinsic material thermal conductivity) according to

$$\kappa_{\text{poly}}^{-1} = \kappa_{\text{bulk}}^{-1} + R_K / \bar{d} \quad (1)$$

Here, we find the same $R_K = 3.8 \times 10^{-7} \text{ m}^2 \text{ K W}^{-1}$ value can completely account for the reduction in thermal conductivity due to the grain size of CG-0, CG-15, and CG-30 samples (Fig. 4c), which have the same filling fraction. The κ_{bulk} value is expected to be different for different dopants and filling fractions. Not only can relevant phonon scattering processes (e.g. phonon-phonon, electron-phonon, and point defect) change, but the phonon group velocity (e.g. speed of sound) is known to change with filling fraction in Yb-doped CoSb_3 (Fig. S4, Supporting Information) [32]. In fact, several compositions with different Yb filling fractions were prepared. The effect of adding Yb from 0.2 to ≥ 0.3 reduces the lattice thermal conductivity by $\sim 25\%$ without CG (Fig. 4d), i.e. a reduction in κ_{bulk} . To mitigate Yb loss, a CG processing time of 30 min was used. The CG processing step reduces κ_{lat} by $\sim 25\%$ for all

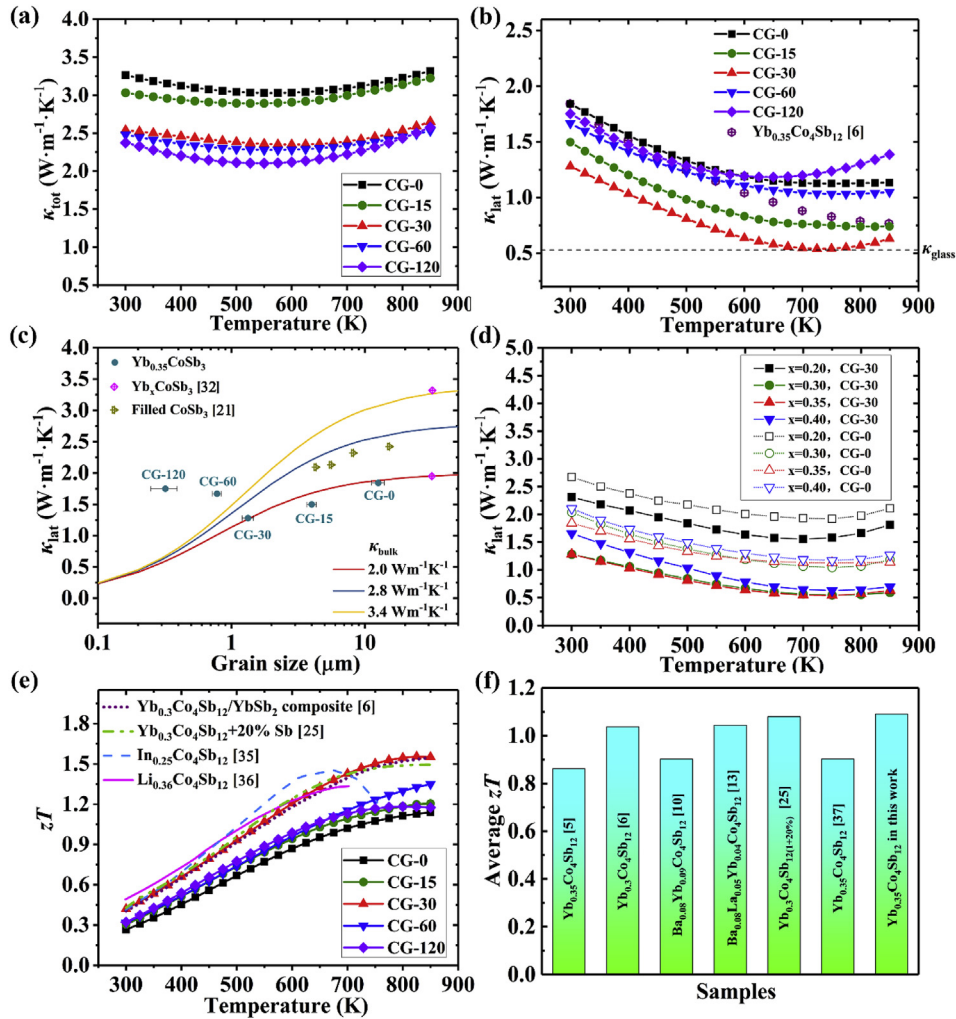


Fig. 4. Temperature dependence of thermal transport properties (a) total thermal conductivity (κ_{tot}) and (b) estimated lattice thermal conductivity (κ_{lat}) of the bulk $\text{Yb}_{0.35}\text{Co}_4\text{Sb}_{12}$ samples with different CG time. (c) estimated κ_{lat} as function of grain size (Eq. (1)) of the bulk $\text{Yb}_{0.35}\text{Co}_4\text{Sb}_{12}$ and $\text{Yb}_{0.2}\text{Co}_4\text{Sb}_{12}$ samples with different CG time. Some reported data are included for comparison. (d) Temperature-dependent lattice thermal conductivity of the $\text{Yb}_x\text{Co}_4\text{Sb}_{12}$ ($x = 0.2, 0.3, 0.35, 0.4$) samples prepared without CG process (CG-0) and with CG for 30 min (CG-30). (e) Temperature-dependent zT of the $\text{Yb}_x\text{Co}_4\text{Sb}_{12}$ samples and several typical data from the Refs. [6,25,35,36] and (f) comparison of the average zT values in the range of 300–850 K in this work with other reported values [5,6,10,13,25,37].

compositions, in agreement with the trend predicted by Equation (1). Thus, for materials with similar compositions, having a similar value of κ_{bulk} , the trend with grain size is well described using the same value of R_{κ} .

While making the grain size continually smaller is expected to reduce thermal conductivity (Eq. (1)), here we find that the apparent κ_{lat} of the CG-60 and CG-120 samples is not captured by the model (Fig. 4c). However, this is only a result of the poor electrical mobility in these materials, which is lower than what is expected for their carrier concentration (Fig. 3b) and is indicative of a strong grain boundary effect on electrical conductivity [33]. This drastic impact on electrical conductivity does not necessarily impact thermal conductivity, and thus the Wiedemann-Franz law can overestimate κ_{lat} in such cases. Nevertheless, since these samples have lower Yb content (Fig. 1b), they are expected to have a larger κ_{bulk} than the CG-0, CG-15 or CG-30 materials.

As a higher doped material is also desired for electrical properties, the CG-30 $\text{Yb}_{0.35}\text{Co}_4\text{Sb}_{12}$ sample was found to be the optimized material of this study (see Fig. S5, Supporting Information). Lastly, we note that the CG-30 $\text{Yb}_{0.35}\text{Co}_4\text{Sb}_{12}$ sample has a κ_{lat} that, at high temperatures, approaches the glassy limit of thermal

conductivity (κ_{glass}) of CoSb_3 (Fig. 4b) [13]. Further reductions in thermal conductivity may be possible if the vibrational character of CoSb_3 materials can be made to be more *diffuson*-like [34].

The temperature dependence of zT of all bulk $\text{Yb}_{0.35}\text{Co}_4\text{Sb}_{12}$ samples with different CG time is shown in Fig. 4e. The increased Seebeck coefficients and reduced lattice thermal conductivities result in a notable enhancement of zT values for the whole temperature range. A peak zT of ~ 1.55 at 825 K is reproducibly achieved for the CG-30 sample (see Fig. S3, Supporting Information), which is the highest value among all the reported single-element-filled CoSb_3 materials. As shown in Fig. 4f, the CG-30 sample has an average zT around 1.09 when the cold-side temperature and hot-side temperature are 300 and 850 K, respectively, comparable to the best single- or even three-element-filled SKDs in the literature [5,6,10,13,25,37]. Although average material zT is commonly reported, it is the *device* figure of merit, ZT , that describes the maximum efficiency of a thermoelectric leg in operation. Using the method in Ref. [38], a device $ZT = 0.95$ was determined from the material properties of the CG-30 sample from 300 to 850 K and the corresponding device efficiency is expected to be theoretically 14.7% (see Fig. S6, Supporting Information).

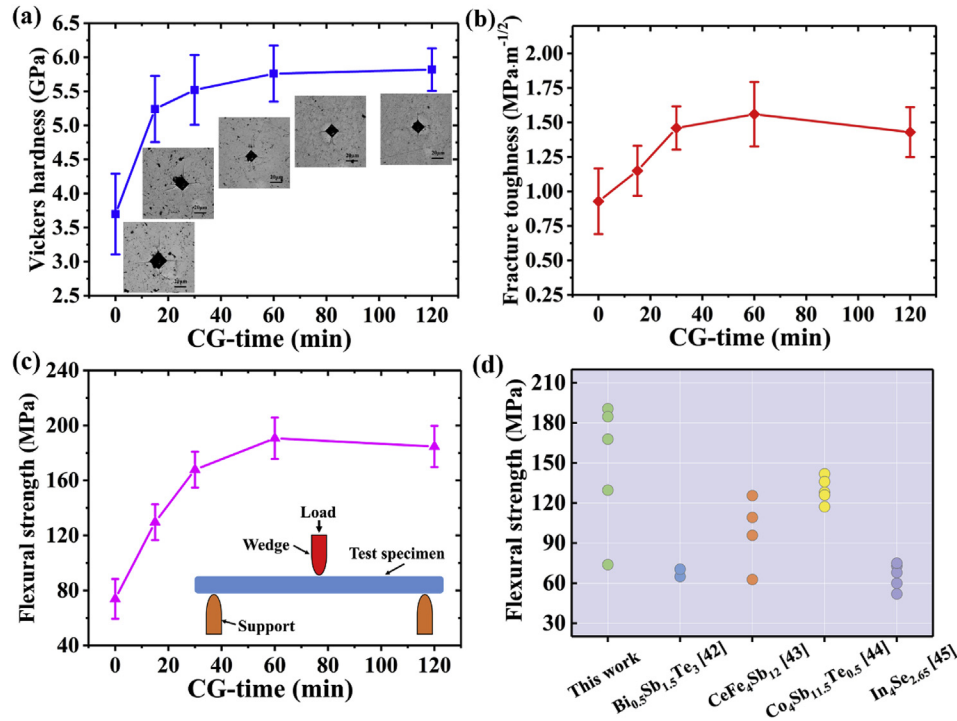


Fig. 5. Mechanical properties of the bulk $\text{Yb}_{0.35}\text{Co}_4\text{Sb}_{12}$ samples as a function of CG time. (a) Vickers hardness with the insets showing the optical microscopy images of indentation; scale bars are 20 μm , (b) fracture toughness, and (c) three-point flexural strength with the inset of the testing schematic diagram. (d) Comparison of three-point flexural strength of CG $\text{Yb}_{0.35}\text{Co}_4\text{Sb}_{12}$ samples in this work with other reported values [42–45].

3.4. Mechanical properties

Superior mechanical properties are beneficial for improving TE material machinability and device reliability. Fig. 5 shows the Vickers hardness, fracture toughness, and three-point flexural strength of all bulk $\text{Yb}_{0.35}\text{Co}_4\text{Sb}_{12}$ samples with different CG time. The Vickers hardness (Fig. 5a) increases with the increasing CG processing time, which can mainly be ascribed to the grain refinement and random distribution of crystallites resulting from the effective cryogenic grinding [39]. The remarkable increase in Vickers hardness can contribute to the enhanced machinability, which is beneficial for manufacturing of TE devices. The fracture toughness (Fig. 5b) reaches the maximum value after CG for 60 min, about 26–50% over that of the $\text{Yb}_{0.35}\text{Co}_4\text{Sb}_{12}$ sample without CG. Three factors may be responsible for the strengthening mechanism: a) the grain size reduction as described by the Hall-Petch relation [40], b) the hierarchical structure [41], and, c) the random crystal orientation [42]. The room-temperature three-point flexural strength is displayed in Fig. 5c. The trend of flexural strength as a function of CG time is similar to that of fracture toughness and hardness, likely because of the same microscopic reasons. The CG-ed samples also have a higher flexural strength than other TE materials (e.g. ~70 MPa for BiSbTe alloy [42], 60–126 MPa for $\text{CeFe}_4\text{Sb}_{12}$ composites [43], 115–140 MPa for $\text{Co}_4\text{Sb}_{11.5}\text{Te}_{0.5}$ nanocomposites [44] and 50–70 MPa for TiC -dispersed $\text{In}_4\text{Se}_{2.65}$ [45] in Fig. 5d). Apparently, the CG process is very effective at improving the mechanical performances of SKD, which grants benefits for material processing and device integration.

4. Conclusions

In summary, optimization of both composition and microstructure can simultaneously tune the electrical, thermal, and

mechanical properties of single-filled skutterudite to rival the thermoelectric performance of multi-filled compounds. By manipulation of the microstructure through cryogenic grinding combined with optimizing Yb filling fraction, a peak zT of 1.55 at 825 K is realized, which is the highest value among all reported single-element-filled CoSb_3 materials; also, an average zT of around 1.09 with a calculated device efficiency of ~14% is reported from 300 to 850 K, comparable to the best result of the multiple-element-filled skutterudite. Furthermore, the high-performance material could be synthesized reproducibly. Simultaneously, the Vickers hardness, fracture toughness and flexural strength are improved. The systematic engineering of this material highlights the realistic prospect of producing high-performance thermoelectric materials with simple composition.

Acknowledgements

This work was funded by Natural Science Foundation of China (Nos. 51774096, 51871053), Shanghai Committee of Science and Technology (Nos. 16JC1401800, 18JC1411200). The contributions of M. T. Agne and G. J. Snyder were supported by the NASA Science Missions Directorate under the Radioisotope Power Systems Program. G. J. Snyder acknowledges support from the National Science Foundation (DMREF-1333335 and DMREF-1729487).

Appendix A. Supplementary data

Supplementary data to this article can be found online at <https://doi.org/10.1016/j.jmat.2019.04.008>.

References

- [1] Shi X, Chen LD. Thermoelectric materials step up. *Nat Mater* 2016;15:691–2.
- [2] He J, Tritt TM. Advances in thermoelectric materials research: looking back

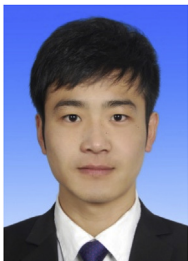
- and moving forward. *Science* 2017;357(6358): eaak9997.
- [3] Shi X, Bai SQ, Xi LL, Yang J, Zhang WQ, Chen LD, et al. Realization of high thermoelectric performance in n-type partially filled skutterudites. *J Mater Res* 2011;26(15):1745–54.
 - [4] Nolas GS, Kaeser M, Littleton RT, Tritt TM. High figure of merit in partially filled ytterbium skutterudite materials. *Appl Phys Lett* 2000;77(12):1855–7.
 - [5] Tang Y, Gibbs ZM, Agapito LA, Li G, Kim HS, Nardelli MB, et al. Convergence of multi-valley bands as the electronic origin of high thermoelectric performance in CoSb_3 skutterudites. *Nat Mater* 2015;14:1223–8.
 - [6] Wang S, Salvador JR, Yang J, Wei P, Duan B, Yang J. High-performance n-type $\text{Yb}_x\text{Co}_4\text{Sb}_{12}$: from partially filled skutterudites towards composite thermoelectrics. *NPG Asia Mater* 2016;8(7):e285.
 - [7] Li H, Tang XF, Su XL, Zhang QJ. Preparation and thermoelectric properties of high-performance Sb additional $\text{Yb}_{0.2}\text{Co}_4\text{Sb}_{12+y}$ bulk materials with nanostructure. *Appl Phys Lett* 2008;92(20):202114.
 - [8] Chen LD, Kawahara T, Tang XF, Goto T, Hirai T, Dyck JS, et al. Anomalous barium filling fraction and n-type thermoelectric performance of $\text{Ba}_x\text{Co}_4\text{Sb}_{12}$. *J Appl Phys* 2001;90(4):1864–8.
 - [9] Pei YZ, Yang J, Chen LD, Zhang W, Salvador JR, Yang J. Improving thermoelectric performance of caged compounds through light-element filling. *Appl Phys Lett* 2009;95(4): 042101.
 - [10] Shi X, Kong H, Li CP, Uher C, Yang J, Salvador JR, et al. Low thermal conductivity and high thermoelectric figure of merit in n-type $\text{Ba}_x\text{Yb}_y\text{Co}_4\text{Sb}_{12}$ double-filled skutterudites. *Appl Phys Lett* 2008;92:182101.
 - [11] Zhao WY, Wei P, Zhang QJ, Dong CL, Liu LS, Tang XF. Enhanced thermoelectric performance in barium and indium double-filled skutterudite bulk materials via orbital hybridization induced by indium filler. *J Am Chem Soc* 2009;131(10):3713–20.
 - [12] Li H, Su XL, Tang XF, Zhang QJ, Uher C, Snyder GJ, et al. Grain boundary engineering with nano-scale InSb producing high performance $\text{In}_x\text{Ce}_y\text{Co}_4\text{Sb}_{12+z}$ skutterudite thermoelectrics. *J Materiomics* 2017;3(4):273–9.
 - [13] Shi X, Yang J, Salvador JR, Chi M, Cho JY, Wang H, et al. Multiple-filled skutterudites: high thermoelectric figure of merit through separately optimizing electrical and thermal transports. *J Am Chem Soc* 2011;133(20):7837–46.
 - [14] Rogl G, Grytsiv A, Rogl P, Peranio N, Bauer E, Zehetbauer M, et al. n-Type skutterudites (R,Ba,Yb) $\text{Co}_4\text{Sb}_{12}$ ($\text{R}=\text{Sr, La, Mm, DD, SrMm, SrDD}$) approaching $\text{ZT} \approx 2.0$. *Acta Mater* 2014;63:30–43.
 - [15] Zhang QH, Zhou ZX, Dylla M, Agne MT, Pei YZ, Wang LJ, et al. Realizing high-performance thermoelectric power generation through grain boundary engineering of skutterudite-based nanocomposites. *Nano Energy* 2017;1: 501–10.
 - [16] Wei TR, Wu CF, Li F, Li JF. Low-cost and environmentally benign selenides as promising thermoelectric materials. *J Materiomics* 2018;4(4):304–20.
 - [17] Li MM, Shao HZ, Xu JT, Wu QS, Tan XJ, Liu GQ, et al. Microstructure engineering beyond $\text{SnSe}_{1-x}\text{S}_x$ solid solution for high thermoelectric performance. *J Materiomics* 2018;4(4):321–8.
 - [18] Su XL, Wei P, Li H, Liu W, Yan Y, Li P, et al. Multi-scale microstructural thermoelectric materials: transport behavior, non-equilibrium preparation, and applications. *Adv Mater* 2017;29(20):1602013.
 - [19] Pan Y, Aydemir U, Grovogui JA, Witting IT, Hanus R, Xu Y, et al. Melt-centrifuged $(\text{Bi,Sb})_2\text{Te}_3$: engineering microstructure toward high thermoelectric efficiency. *Adv Mater* 2018;30:1802016.
 - [20] Hanus R, Agne MT, Rettie AJE, Chen Z, Tan G, Chung DY, et al. Lattice softening significantly reduces thermal conductivity and leads to high thermoelectric efficiency. *Adv Mater* 2019:1900108.
 - [21] Zong PA, Hanus R, Dylla M, Tang Y, Liao J, Zhang QH, et al. Skutterudite with graphene-modified grain-boundary complexion enhances zT enabling high-efficiency thermoelectric device. *Energy Environ Sci* 2017;10(1):183–91.
 - [22] Zhang QH, Liao JC, Tang YS, Gu M, Ming C, Qiu PF, et al. Realizing a thermoelectric conversion efficiency of 12% in bismuth telluride/skutterudite segmented modules through full-parameter optimization and energy-loss minimized integration. *Energy Environ Sci* 2017;10(4):956–63.
 - [23] Xiong Z, Chen X, Huang X, Bai S, Chen L. High thermoelectric performance of $\text{Yb}_{0.26}\text{Co}_4\text{Sb}_{12}/\text{yGaSb}$ nanocomposites originating from scattering electrons of low energy. *Acta Mater* 2010;58(11):3995–4002.
 - [24] Dahal T, Jie Q, Joshi G, Chen S, Guo C, Lan Y, Ren ZF. Thermoelectric property enhancement in Yb-doped n-type skutterudites $\text{Yb}_x\text{Co}_4\text{Sb}_{12}$. *Acta Mater* 2014;75:316–21.
 - [25] Meng X, Liu Z, Cui B, Qin D, Geng H, Cai W, et al. Grain boundary engineering for achieving high thermoelectric performance in n-type skutterudites. *Adv Energy Mater* 2017;7:1602582.
 - [26] Zhao XY, Shi X, Chen LD, Zhang WQ, Bai SQ, Pei YZ, et al. Synthesis of $\text{Yb}_y\text{Co}_4\text{Sb}_{12}/\text{Yb}_2\text{O}_3$ composites and their thermoelectric properties. *Appl Phys Lett* 2006;89(9):092121.
 - [27] Li Y, Qiu P, Xiong Z, Chen J, Nunna R, Shi X, et al. Electrical and thermal transport properties of $\text{Yb}_x\text{Co}_4\text{Sb}_{12}$ filled skutterudites with ultrahigh carrier concentrations. *APL Adv* 2015;5(11):117239.
 - [28] Tang Y, Chen SW, Snyder GJ. Temperature dependent solubility of Yb in Yb-CoSb_3 skutterudite and its effect on preparation, optimization and lifetime of thermoelectrics. *J Materiomics* 2015;1(1):75–84.
 - [29] ASTM E112–13. Standard test methods for determining average grain size. West Conshohocken, PA: ASTM International; 2013.
 - [30] Zong PA, Chen XH, Zhu Y, Liu Z, Zeng Y, Chen LD. Construction of a 3D-rGO network-wrapping architecture in a $\text{Yb}_y\text{Co}_4\text{Sb}_{12}/\text{rGO}$ composite for enhancing the thermoelectric performance. *J Mater Chem* 2015;3:8643–9.
 - [31] Ding J, Gu H, Qiu P, Chen X, Xiong Z, Zheng Q, et al. Creation of Yb_2O_3 Nanoprecipitates through an oxidation process in bulk Yb-filled skutterudites. *J Electron Mater* 2013;42:382–8.
 - [32] Tang YL. PhD Thesis12. California Institute of Technology; 2015.
 - [33] Kuo JJ, Kang SD, Imasato K, Tamaki H, Ohno S, Kanno T, et al. Grain boundary dominated charge transport in Mg_3Sb_2 -based compounds. *Energy Environ Sci* 2018;11(2):429–34.
 - [34] Agne MT, Hanus R, Snyder GJ. Minimum thermal conductivity in the context of diffusion-mediated thermal transport. *Energy Environ Sci* 2018;11(3): 609–16.
 - [35] Benyahia M, Ohorodniichuk V, Leroy E, Dauscher A, Lenoir B, Alleno E. High thermoelectric figure of merit in mesostructured $\text{In}_{0.25}\text{Co}_4\text{Sb}_{12}$ n-type skutterudite. *J Alloy Comp* 2018;735:1096–104.
 - [36] Zhang J, Xu B, Wang L-M, Yu D, Yang J, Yu F, et al. High-pressure synthesis of phonon-glass electron-crystal featured thermoelectric $\text{Li}_x\text{Co}_4\text{Sb}_{12}$. *Acta Mater* 2012;60(3):1246–51.
 - [37] Yang J, Hao Q, Wang H, Lan YC, He QY, Minnich A, et al. Solubility study of Yb inn-type skutterudites $\text{Yb}_x\text{Co}_4\text{Sb}_{12}$ and their enhanced thermoelectric properties. *Phys Rev B* 2009;80:115329.
 - [38] Snyder GJ, Snyder AH. Figure of merit ZT of a thermoelectric device defined from materials properties. *Energy Environ Sci* 2017;10:2280–3.
 - [39] Matsuura K, Kata DB, Lis JT, Kudoh M. Grain refinement and improvement in mechanical properties of Nb–Al–Si intermetallic alloys. *ISIJ Int* 2006;46:875–9.
 - [40] Wachtman JB, Cannon WR, Mathewson MJ. Mechanical properties of ceramics. John Wiley & Sons; 2009.
 - [41] Habibi MK, Gupta M, Joshi SP. Size-effects in textural strengthening of hierarchical magnesium nano-composites. *Mater Sci Eng A-Struct Mater* 2012;556:855–63.
 - [42] Zheng Y, Zhang Q, Su X, Xie H, Shu S, Chen T, et al. Mechanically robust BiSbTe alloys with superior thermoelectric performance: a case study of stable hierarchical nanostructured thermoelectric materials. *Adv Energy Mater* 2015;5:1401391.
 - [43] Wan S, Huang X, Qiu P, Bai S, Chen L. The effect of short carbon fibers on the thermoelectric and mechanical properties of p-type $\text{CeFe}_4\text{Sb}_{12}$ skutterudite composites. *Mater Des* 2015;67:379–84.
 - [44] Duan B, Zhai P, Ding S, Xu C, Li G, Liu L, et al. Effects of nanoparticle size on the thermoelectric and mechanical properties of skutterudite nanocomposites. *J Electron Mater* 2014;43(6):2115–20.
 - [45] Li G, Yang J, Xiao Y, Fu L, Luo Y, Zhang D, et al. Effect of TiC nano inclusions on thermoelectric and mechanical performance of polycrystalline $\text{In}_4\text{Se}_{2.65}$. *J Am Ceram Soc* 2015;98(12):3813–7.



Zhenxing Zhou received his B.E. degree from Donghua University, China in 2012. He is currently studying for a Ph.D. degree in State Key Laboratory for Modification of Chemical Fibers and Polymer Materials, College of Materials Science and Engineering at Donghua University. He is working on the processing of micro/nanostructured thermoelectric composites by high energetic milling, cryogenic grinding and SPS in order to improve the thermoelectric properties for high-performance power generation devices.



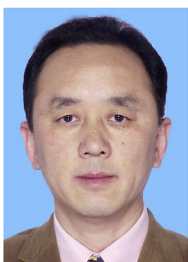
Matthias T. Agne received his Bachelor and Master degrees in Materials Science and Engineering from Drexel University in 2015, having worked with MAX phase ceramic materials under Professor Michel Barsoum. Now he is pursuing his PhD under the advisory of Professor G. Jeffrey Snyder at Northwestern University. His current research is concentrated in thermodynamics and materials physics, with applications to thermal transport, thermoelectric materials and measurements.



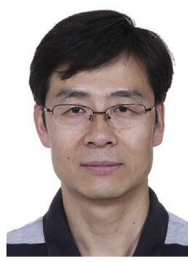
Qihao Zhang is currently a research associate at Shanghai Institute of Ceramics, Chinese Academy of Sciences (SICCAS). He received his Ph.D. from SICCAS under the advisory of Prof. Lidong Chen in 2018. His current research focuses on the development of advanced thermoelectric nanocomposites and design, fabrication and evaluation of thermoelectric power generation devices and systems.



G. Jeffrey Snyder is a Professor of Materials Science and Engineering at Northwestern University in Evanston Illinois. His interests are focused on the materials physics and chemistry for thermoelectric engineering, such as band engineering, design of complex Zintl compounds and use of nanostructured composites. His interdisciplinary approach stems from studies of Solid State Chemistry at Cornell University and the Max Planck Institute for solid state research, Applied Physics at Stanford University and thermoelectric materials & device engineering at NASA/Jet Propulsion Laboratory and California Institute of Technology (Caltech).



Wan Jiang is a Professor of Donghua University and Director of the Engineering Research Center of AGMT. He received his B.S. from Dalian University of Technology in China (1983) and Ph.D. from Tohoku University in Japan (1994). He gained the “Hundreds Talent Project” in Chinese Academy of Sciences in 1999 and National Science Fund for Distinguished Young Scholars in 2006. His research activities are focused on low cost and fast in-situ synthesis/sintering of nano-ceramic composites, thermoelectric materials and fabrication of functional glass by SPS.



Lianjun Wang obtained his Ph.D. degree from Dalian University of Technology in 2002 and then worked as postdoctoral research fellow at Shanghai Institute of Ceramics, Chinese Academy of Sciences and University of Stockholm. He joined Donghua University as a professor in 2010. He has gained multiple talent supporting programs including New Century Talent Supporting Project by education ministry, Shanghai Science and Technology Development Funds, the Dawn Program of Shanghai Education, Shanghai outstanding technical leaders plan. He specializes in thermoelectric materials, sintering preparation and photoelectric properties of bulk functional glass, micro/nanostructured bulk materials and advanced ceramics.